Proceedings of ASME 2019 International Design Engineering Technical Conferences & Computers and Information in Engineering Conference
IDETC/CIE 2019
Aug 18-21, 2019, Anaheim, CA, USA

IDETC2019-97420

EXPLOITING THE ASYMMETRIC ENERGY BARRIER IN MULTI-STABLE ORIGAMI TO ENABLE MECHANICAL DIODE BEHAVIOR IN COMPRESSION

Nasim Baharisangari and Suyi Li*
Department of Mechanical Engineering
Clemson University, Clemson, SC, USA

ABSTRACT

Recently, multi-stable origami structures and material systems have shown promising potentials to achieve multi-functionality. Especially, origami folding is fundamentally a three-dimensional mechanism, which imparts unique capabilities not seen in the more traditional multi-stable systems. This paper proposes and analytically examines a multi-stable origami cellular structure that can exhibit asymmetric energy barriers and a mechanical diode behavior in compression. Such a structure consists of many stacked Miura-ori sheets of different folding stiffness and accordion-shaped connecting sheets, and it can be divided into unit cells that features two different stable equilibria. To understand the desired diode behavior, this study focuses on two adjacent unit cells and examines how folding can create a kinematic constraint onto the deformation of these two cells. Via estimating the elastic potential energy landscape of this dual cell system. we find that the folding-induced kinematic constraint can significantly increase the potential energy barrier for compressing the dual-cell structure from a certain stable state to another, however, the same constraint would not increase the energy barrier of the opposite extension switch. As a result, one needs to apply a large force to compress the origami cellular structure but only a small force to stretch it, hence a mechanical diode behavior. Results of this study can open new possibilities for achieving structural motion rectifying, wave propagation control, and embedded mechanical computation.

***Keywords**: Origami, Multi-Stability, Mechanical Diode*

1. INTRODUCTION

A structure or material system is considered multi-stable if they exhibit more than one stable equilibrium (or stable state) within the deformation range so that each state corresponds to a potential energy minimum [1]. Exploiting the multi-stability can lead to a wide variety of adaptive functionalities including stiffness adaptation [2], energy harvesting [3,4], impact energy absorption [5–7], and robust sensing [8,9] etc. Therefore, multi-stability is a powerful catalyst for constructing smart and multi-functional structures and material systems. Over the past several decades, many mechanisms, such as the buckled beams and asymmetric fiber laminates [10], have been examined extensively as building blocks for achieving multi-stability.

Recently, origami-based cellular structures and materials have emerged as promising platforms to achieve multi-stability [11]. Such structures and materials typically consist of multiple origami sheets, and they have shown many unique mechanical properties such as negative Poisson's ratio [12–14], discrete stiffness jumps [15,16], and high load-bearing capacity [17]. Moreover, multi-stability would arise in origami if its crease lines have different stiffness [18,19], or its facets are deformed between different folding configurations [20–22]. One example of a multi-stable origami structure is the stacked Miura-*ori*, which is constructed by assembling geometrically compatible Miura-*ori* sheets along their crease lines. If the stiffness of these Miura-*ori* sheets is significantly different from each other, multi-stability will occur. By combining this multi-stability and the three-dimensional nature of origami folding, the stacked Miura-*ori* has been shown to exhibit rapid deformation via pressure-induced snapping [19] and elastic modulus programming [23].

Moreover, the multi-stable stacked Miura-*ori* also exhibits unique asymmetric energy barriers and mechanical diode behavior [24]. That is, the kinematic constraint from folding can significantly increase the potential energy barrier for *stretching* the stacked Miura-*ori* from one stable state to another, but does not notably increase the energy barrier for the opposite *compression* switch. As a result, one must apply a very large force to stretch

* Address all correspondence to this author: suyil@clemson.edu

the stacked Miura-*ori* but only a small force to compress it, hence a static diode behavior. However, the stacked Miura-*ori* cellular structure can only exhibit such an increase in potential energy barrier in extension, which naturally leads to the research question of this study: *How to achieve a similar diode behavior in compression, so that one must apply a large force to compress the origami structure but only a small force to extend it?*

In this study, we propose and analyze a new origami cellular structure design that exhibits the desired asymmetric energy barrier and mechanical diode behavior in compression. This new design can be considered as a variation of the stacked Miura-*ori* in that the arrangement of different Miura-*ori* sheet is reversed. By calculating the potential energy landscape of this new cellular structure using rigid facet and spring hinge crease assumption, we show that the kinematic constraints from folding can significantly increase the potential energy barrier for a compression switch between stable states, but do not notably increase the energy barrier for the opposite extension switch. Results of this study can lay down the foundation for multi-functional origami structure and materials that can perform motion rectifying, wave propagation control, and embedded mechanical computation.

In what follows, section 2 briefly reviews the diode behavior in tension; section 3 presents the new cellular origami structure design and physical principles of analyzing its potential energy; section 4 details the asymmetric energy barrier and mechanical diode behavior in compression; and finally, section 5 concludes this paper with summary and discussion.

2. Brief Review of the Diode Effect in Tension

The authors' previous study examined the nonlinear elastic behaviors of a stacked Miura-*ori* cellular structure, and the diode effect occurs between two bistable unit cells connected along their zig-zag crease (Figure 1(a)). Each unit cell can settle into two different stable states, which are denoted as the state (0) and (1), respectively. Thus, the dual-cell assembly has four unique stable states: (00), (01), (10), and (00). Rigid-folding of Miura-ori is fundamentally a three-dimensional motion, which imposes a kinematic constraint onto the deformation of these two unit cells. That is, the "spine angle" defined by the zig-zag connecting crease should be equal between the two cells (aka. $\psi^{A} = \psi^{B}$ in Figure 1(a)). Such a kinematic constraint was found to significantly increase the potential energy barrier for the extension switch from (01) to (00) stable states, however, it does not impose any notable change to the energy barrier for the opposite compression switch from (00) back to (01) state.

This unorthodox behavior was illustrated in a set of tests. In these tests, two bistable unit cell prototypes were connected by two different setups and their overall force-deformation curves were measured using a universal test machine. In one setup, the unit cells were connected via a rigid rod, so that they were connected simply in series without reinforcing any kinematic constraint of folding (aka. ψ^{A} and ψ^{B} were independent). In the other setup, the unit cells were directly connected along their zig-zag creases using adhesive films to reinforce the kinematic constraint (aka. $\psi^{A} \cong \psi^{B}$ with a small mismatch).

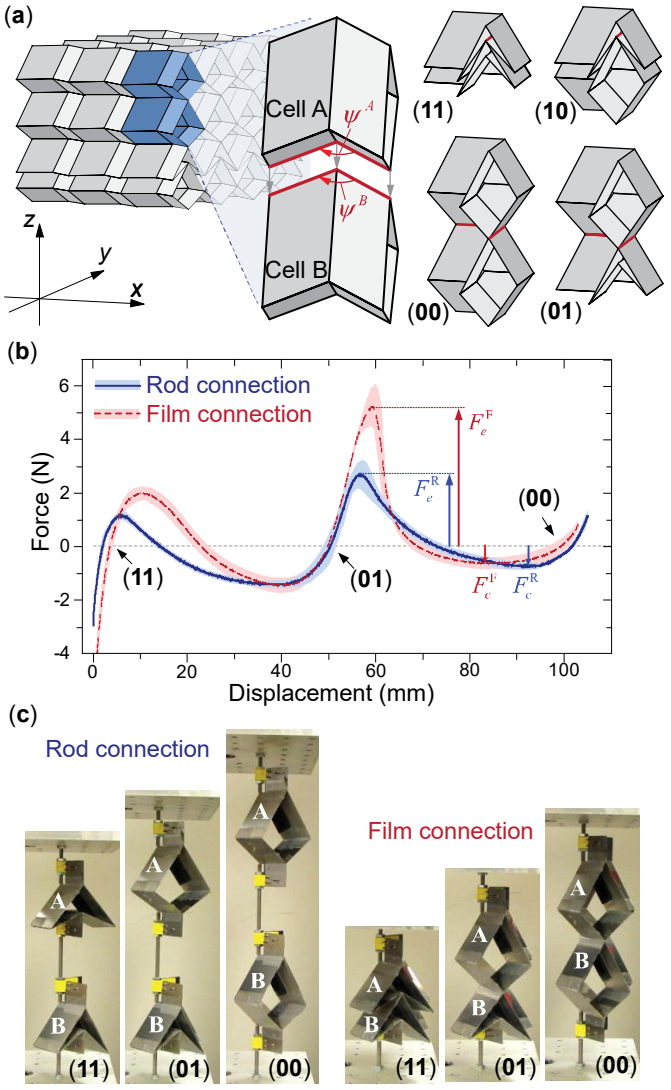

Figure 1. A review of the mechanical diode behavior in tension. (a) The classical stacked Miura-*ori* cellular structure. The examined dual-cell assembly is highlighted here, together with the four stable states it can settle into. (b) Measured force-displacement curves showing the mechanical diode effect. Here, the solid lines are the averaged results of a loading and unloading cycle, and the shaded bands are the standard deviation. (c) The dual cell assembly prototypes at the different stable states observed in the experiments. Figures adapted with permission from [24]. Copyright: Elsevier.

The dual cell assemblies in both setups could be switched in-between (11), (01), and (00) stable states as their overall length was extended or compressed by the tester machine. However, the maximum extension force from (01) and (00) stable state was much higher in the second setup with reinforced kinematic constraint (aka. $F_e^F > F_e^R$ in Figure 1(b)). On the other hand, the compression forces in the opposite switch from (00)

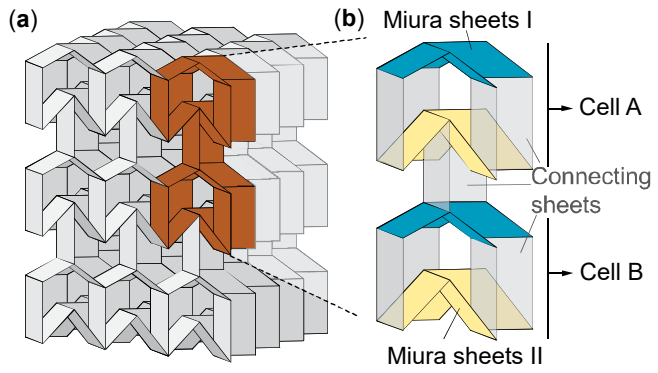

Figure 2: Design of the new multi-stable stacked origami cellular structure. (a) An overview showing the alternating sequence of different Miura-*ori* sheets and zig-zag "connect sheets". (b) A close-up view of the dual-cell pair, which is the most fundamental unit to achieve the diode behavior in compression.

back to (01) were similar between the two setups ($F_c^F \cong F_c^R$). Therefore, the kinematic constraint of Miura-*ori* rigid-folding creates a mechanical diode effect that makes it hard to extend the stacked Miura-ori cellular structure but easy to compress it. Further analytical investigation predicted that the strength of such a diode effect would further increase if the kinematic constraint is strictly reinforced by reducing the mismatch between the two spine angles ψ^A and ψ^B.

While promising, the diode behavior in the classical stacked Miura-ori cellular structure is available only in extension. This leads to the research question of this study: How to achieve a diode behavior in compression and construct a cellular structure that is easy to be extended but hard to compress? This question is addressed in the following sections.

3. Design of the New Cellular Origami Structure

In this study, we propose a new multi-stable cellular origami structure, which is constructed by stacking geometrically compatible Miura-*ori* sheets and zig-zag shaped "connect sheets" in an alternating arrangement (Figure 2(a)). The most fundamental component that can exhibit the desired mechanical diode effect in compression consists of two unit cells and one connect sheet (Figure 2(b)). The unit cell here is essentially a variation of the unit cell used in the previous study on the extension diode because the arrangement of Miura-*ori* sheet I and II are reversed. Therefore, the geometric design principles and rigid-folding kinematics of traditional Miura-*ori* still apply in this study. The crease design of a unit cell is determined by crease lengths (a_I, a_{II}, b_I, b_{II}, and l_c) and sector angles (γ_I, γ_{II}) (Figure 3(a)). Here, subscript I and II denotes the two different Miura-*ori* sheets in a unit cell and l_c is the length of the connecting sheet. To ensure geometric compatibility, these design parameters must satisfy the following relationships [12]:

$$b_{II} = b_I, \tag{1}$$

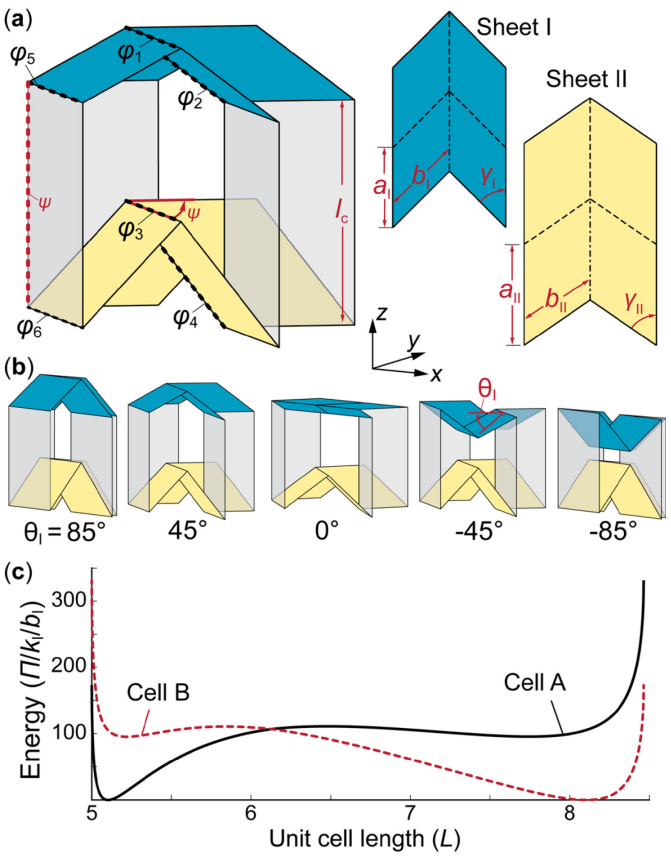

Figure 3: Detailed design of a unit cell in this study. (a) φ_i (I = 1…6) are unique dihedral angles between two adjacent facets along the difference creases. ψ is the spine angle, which is also the dihedral angle of in the connect sheet. The two drawings on the right show the design of Miura-*ori* sheets when they are unfolded into a flat sheet. (b) The external geometries of the unit cell at different θ_I folding angles. Not shown in this plot are the folding angle θ_{II}, which is the dihedral angle between the facets of Miura sheets II and the *x*-*y* reference plane. (c) The energy landscape of the two unit cells used in this study.

$$\frac{\cos\gamma_{II}}{\cos\gamma_I} = \frac{a_I}{a_{II}}. \tag{2}$$

To describe the external geometry of a unit cell during rigid-folding, one can use dihedral *folding angles* θ_I and θ_{II} defined between the facets of two Miura-*ori* sheets and the *x*-*y* reference plane, respectively (Figure 3(b)). We assume the unit cell strictly follows the kinematics of rigid-folding, which is essentially a one-degree-of-freedom motion. Hence the two folding angels are not independent but rather satisfy the geometric relationship:

$$\cos\theta_I \tan\gamma_I = \cos\theta_{II} \tan\gamma_{II}. \tag{3}$$

The external total length of a unit cell along the *z*-axis is simply a summation of its different components so that

$$L = l_{\mathrm{I}} + l_{\mathrm{II}} + l_c, \tag{4}$$

where l_{I} and l_{II} are the length of the two constituent Miura-ori sheets, respectively ($l_{\mathrm{I}} = a_{\mathrm{I}} \sin\theta_{\mathrm{I}} \sin\gamma_{\mathrm{I}}$, $l_{\mathrm{II}} = a_{\mathrm{II}} \sin\theta_{\mathrm{II}} \sin\gamma_{\mathrm{II}}$).

A *spine angle* ψ can be defined to describe dihedral folding angles between the facets in the connect sheet:

$$\psi = 2\tan^{-1}(\cos\theta_{\mathrm{I}} \tan\gamma_{\mathrm{I}}), \tag{5}$$

Since the unit cells are assumed to satisfy the kinematics of rigid-folding, we assume that the facets are rigid and the crease lines act like perfect hinges with prescribed torsional stiffness. Therefore, the total elastic potential energy a unit cell is the summation of the crease torsional spring energy:

$$\Pi = \frac{1}{2}k_i\left(\varphi_i - \varphi_i^o\right)^2 + \frac{1}{2}k_c\left(\psi - \psi^o\right)^2, \tag{6}$$

where φ_i is the dihedral crease opening angle denoted in Figure 3; k_i is the corresponding torsional spring stiffness; and k_c is the torsional crease stiffness in the connect sheets. Angles with the superscript *o* represents the initial stress-free configuration. The magnitudes of the crease opening angles are also functions of the independent variable θ_{I} so that

$$\varphi_{\mathrm{I}} = \pi - 2\theta_{\mathrm{I}}, \tag{7}$$

$$\varphi_2 = 2\sin^{-1}\left(\frac{\cos\theta_{\mathrm{I}}}{\sqrt{1-\sin^2\theta_{\mathrm{I}}\sin^2\gamma_{\mathrm{I}}}}\right), \tag{8}$$

$$\varphi_3 = \pi - 2\cos^{-1}\left(\tan\gamma_{\mathrm{II}} \tan^{-1}\gamma_{\mathrm{I}} \cos\theta_{\mathrm{I}}\right), \tag{9}$$

$$\varphi_4 = 2\sin^{-1}\left(\frac{\sin\gamma_{\mathrm{I}}}{\sin\gamma_{\mathrm{II}}}\sin\frac{\varphi_2}{2}\right), \tag{10}$$

$$\varphi_5 = \frac{\pi}{2} + \theta_{\mathrm{I}}. \tag{11}$$

$$\varphi_6 = \frac{\pi}{2} - \theta_{\mathrm{II}}. \tag{12}$$

Although the torsional springs added to the creases are linearly elastic as shown in Equation 6, the corrections between folding and external deformation are geometric and strongly nonlinear. This nonlinearity is the origin of the desired diode behavior. Denote k_{I} and k_{II} as the crease torsional spring stiffness *per unit length* of the Miura-*ori* sheet I and II, respectively, and k_c is the crease torsional spring stiffness *per unit length* of the connecting sheet. The stiffness coefficients in equation (6) are: $k_1 = 2k_{\mathrm{I}}b_{\mathrm{I}}$, $k_2 = 2k_{\mathrm{I}}a_{\mathrm{I}}$, $k_3 = 2k_{\mathrm{II}}b_{\mathrm{I}}$, $k_4 = 2k_{\mathrm{II}}a_{\mathrm{II}}$, $k_5 = 4k_cb_{\mathrm{I}}$, $k_6 = 4k_cb_{\mathrm{I}}$, and $k_c = 2k_cl_c$, where the numerical constants in these equations represent the number of similar creases in one unit cell.

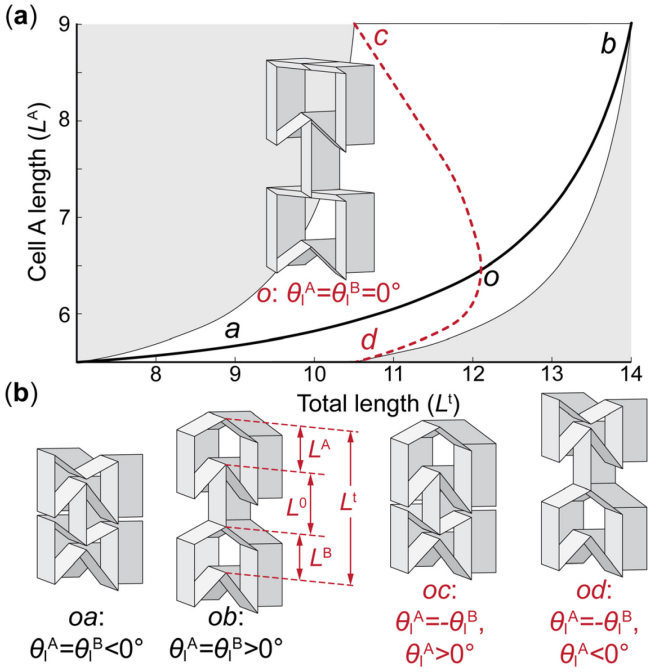

Figure 4: Kinematic properties due to the folding induced constraint (or the lack of). (a) Admissible deformation of the dual cell assembly. The two kinematic paths based on ideal rigid-folding condition are shown by the solid and dashed curves. The gray area represents deformations that are not kinematically admissible. (b) The geometry of the dual cell assembly at different locations along these to kinematic paths.

To achieve bi-stability in a unit cell, the crease stiffness of the larger Miura-*ori* sheet II must be significantly higher than sheet than those of sheet I and connecting sheet (aka. $k_{\mathrm{II}} > k_{\mathrm{I}}$ and $k_{\mathrm{II}} > k_c$). In addition, the initial stress-free folding angle (θ_{I}) must deviate from 0°. Figure 3(c) illustrates the energy landscape of two unit cells (designated as A and B hereafter) corresponding to $a_{\mathrm{I}} = b_{\mathrm{I}} = 2\mathrm{cm}$, $a_{\mathrm{II}} = 1.25a_{\mathrm{I}}$, $\gamma_{\mathrm{I}} = 45^\circ$, $l_c = 2.5\mathrm{a}_{\mathrm{I}}$, $k_{\mathrm{I}} = k_c$, and $k_{\mathrm{II}} = 20k_{\mathrm{I}}$. The initial folding angle $\theta_{\mathrm{I}}^o = -60^\circ$ for unit cell A and 60° for cell B. The bi-stability, characterized by the two potential energy wells, is evident based on these unit cell designs. For clarity, we denote the stable state with a positive sheet I folding angle as the state (1) and the one with the negative sheet I folding angle as the state (0), so that the unit cell has a shorter length *L* at state (0) than the state (1). Unless noted otherwise, these design variables are used throughout this paper.

Once the external geometry and potential energy of a unit cell is formulated, the overall energy and dimension of the dual-cell assembly can be calculated as

$$\Pi^{\mathrm{t}} = \Pi^{\mathrm{A}} + \Pi^{\mathrm{B}} + \Pi^{0}, \tag{13}$$

$$L^{t} = L^{A} + L^{B} + L^{0}. \tag{14}$$

In equation (13), Π^{A} and Π^{B} are the strain energy of the unit cell A and B defined in equation (6), respectively. Π^{0} is the strain energy of the connect sheet in-between two unit cells, and it is estimated as

$$\Pi^{0} = \frac{1}{2} k^{*} \left(\psi^{A} - \psi^{B} \right)^{2}, \tag{15}$$

where k^{*} is the "constraint stiffness" of the connecting sheet.

The magnitude of this constraint stiffness is crucial in this study because it characterizes the strength of the kinematical constraint due to folding. If the kinematics of rigid-folding is strictly followed (aka, all facets in the dual cell assembly are rigid and all creases behave like perfect hinges), the spine angle of the unit cells should be equal, i.e. $\psi^{A} = \psi^{B}$. In this way, the admissible deformations of the dual-cell assembly are limited to two "kinematic paths" shown in Figure 4. On one path, the folding angles of two unit cells are equal (aka. $\theta_{I} = \theta_{II}$); on the other path, the two folding angles have the same magnitude but opposite sign ($\theta_{I} = -\theta_{II}$). However, in realistic scenarios, there would be some mismatch between the two spine angles due to small facet bending or crease wrapping. Therefore, the configuration of the dual-cell assembly can occur at any location within the curved parallelogram shown in Figure 4. *However, such a deviation from the ideal rigid-folding can induce additional strain energy, which can be characterized by the constraint stiffness* k^{*}. It is worth highlighting that this constraint stiffness concept was introduced in the authors' previous study on extension diode and was able to explain the experimental observations [24]. Thus, we will apply it to the compression diode study here. In the following sections, we first examine the nonlinear elastic behaviors of this dual-cell assembly without imposing any kinematic constraint from folding (aka. $k^{*} = 0$) and then examine the effects from an increasingly stronger constraint ($k^{*} > 0$).

4. Diode Effect in Compression

Figure 5(a) illustrates the total energy landscape of the dual cell assembly according to equation (13) assuming $k^{*} = 0$. This corresponds to a hypothetical case that the connecting sheets between the two unit cells are soft in that they do not provide any resistance to the mismatch between the two spine angles ψ^{A} and ψ^{B}. From this plot, one can identify "equilibrium paths" corresponding to the potential energy minima at a given total length. These are paths of deformation that the dual-cell assembly would follow when its total length is increased or decreased. Here, we focus on the continuous equilibrium path that connects three stable states of (00), (01), and (11). The energy landscape of the dual cell assembly along this equilibrium path is plotted in Figure 5(b). Based on this plot, one can identify the potential energy barrier (ΔE_{e}) for the extension switch from (00) stable state to the (01) state and the energy barrier (ΔE_{c}) for the opposite

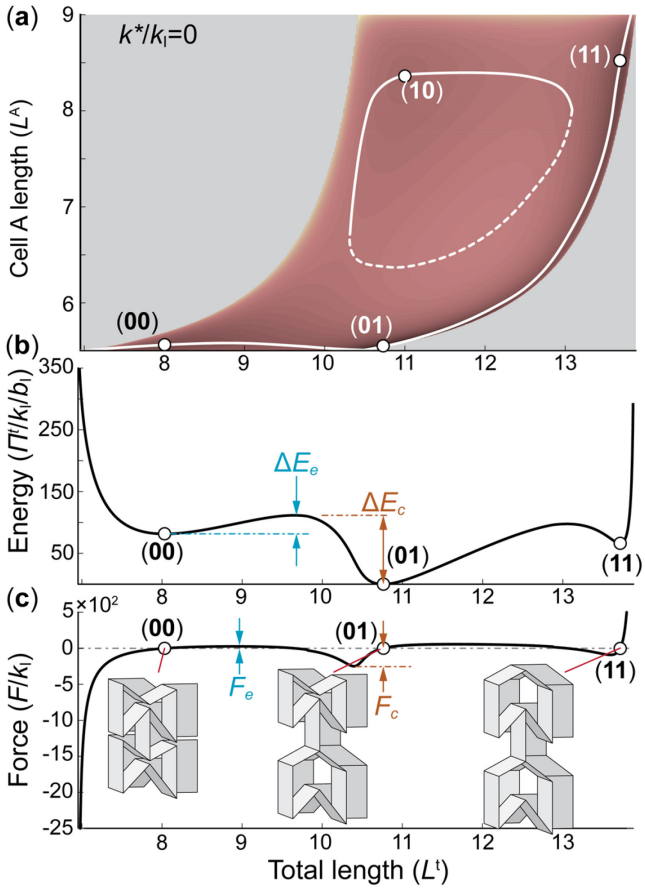

Figure 5: Mechanics of the dual-cell assembly assuming zero constraint stiffness k^{*}: (a) the total potential energy landscape, (b) the equilibrium path, and (c) the reaction force along the equilibrium path. The colormap in (a) represents the total potential energy, darker color means lower energy. It is worth nothing that in this figure and the following Figure 6, only the equilibrium path containing the (00), (01), and (11) stable states are shown in the energy landscape and reaction force plots. This is because the (10) state is not achievable by global extension or compression.

compression switch from (01) to (00). The corresponding reaction force, shown in Figure 5(c), is calculated as the variation of total potential energy with respect to the change in total length,

$$F = \frac{\partial \Pi^{t}}{\partial L^{t}}. \tag{16}$$

Based on the reaction force plot, one can calculate two important forces: One is the critical reaction force (F_{e}) during the extension switch from the (00) stable state to (01); the other is the critical force (F_{c}) during the opposite switch from (01) to (00). Essentially, F_{e} is the required extension force to stretch the dual cell assembly from the (00) state to (01), while F_{c} is the required force to compress this assembly back to the (00) state.

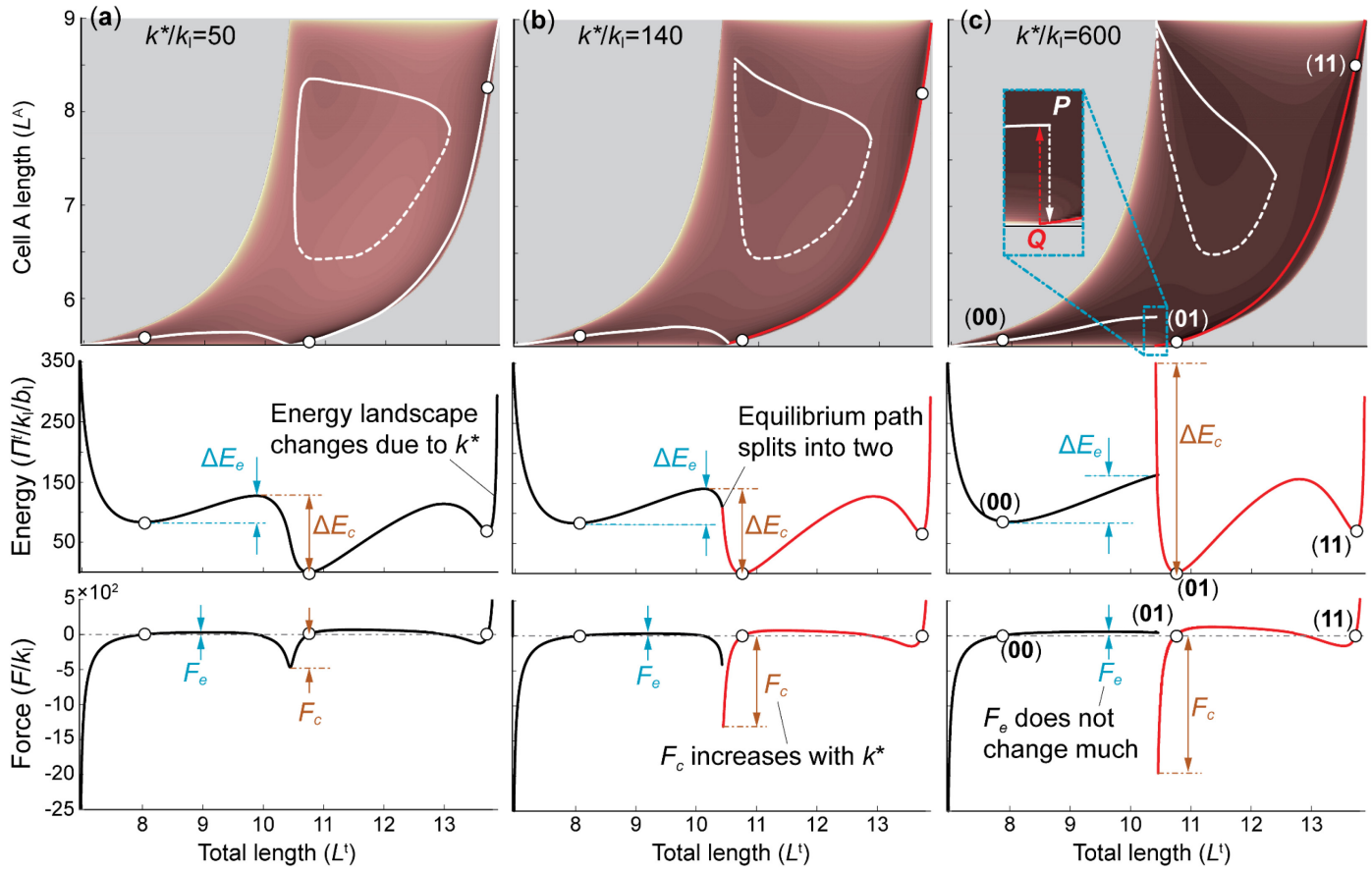

Figure 6: The energy contours (first row), energy landscapes (second row), and the reaction force (third row) corresponding to an increasingly stronger folding induced kinematic constraint: (a) k^*/k_l=50, (b) k^*/k_l=140, and (c) k^*/k_l=600. The "jump" between the equilibrium paths are illustrated as dashed arrows in the insert figure in the first row of (c).

Figure 6 illustrates the potential energy landscape and reaction force of the dual cell assembly when the constraint stiffness k^* increases, which realistically represents the structural behavior of dual cell assembly under external loads. Typically, stiffer connect sheets between two unit cells can strengthen the kinematic constraints due to folding, thus gives a higher constraint stiffness k^*. As the constraint stiffness increases, the potential energy barrier for compression switch from (01) stable state to (00) increases significantly, however, the energy barrier for the extension switch does not increase by the same degree. Moreover, when the constraint stiffness reaches a threshold value ($k^*/k_l = 140$ in this case study), the initially continuous equilibrium path that connects three stable states splits into to separated ones (see the first two rows of Figure 6(b, c)). As a result, as the dual cell assembly is stretched from the (00) stable state, it will deform to point P at the end of one equilibrium path and then "jump" to the other path. Similarly, when the dual cell assembly is compressed from the (01) stable state, it will deform to point Q first before jumping (see the insert figure in the first row if Figure 6(c)). The energy barrier for reaching these jumps are significantly different between extension and compression, therefore, the kinematic constraint due to folding imposes an asymmetry in the energy barriers of the dual cell assembly.

Such asymmetry can be further illustrated by examining the changes in critical reaction forces as the constraint stiffness k^* increases (the third-row Figure 6). That is, when k^* increases, the required force for the compression switch from (01) stable state to (00) increases significantly, while the required extension force for the opposite extension switch from (00) to (10) does not increase much (Table 1). Essentially, the kinematic constraint of folding induces a mechanical diode effect so that the stacked origami cellular structure can be stretched easily but hard to be compressed.

Table 1. The normalized critical forces in the extension and compression switches between the (00) and (01) stable states based on the reaction force plots in Figure 5 and 6.

k^*/k_l	F_e/k_l	F_c/k_l
0	26.5	-91.7
50	32.5	-467.3
140	36.3	-1261.7
600	39.9	-2079.7

5. Summary and Conclusion

This study proposes and analytically examines a multi-stable, cellular origami structure that can exhibit an asymmetric energy barrier and mechanical diode behavior in compression. Such a cellular structure consists of multiple unit cells, each of which is made by stacking two different Miura-*ori* sheets and accordion-shaped connecting sheets. These unit cells can be bistable due to the nonlinear correlations between folding and crease deformation. This study focuses on a dual cell assembly, which is the most fundamental structure to achieve the desired mechanical diode behavior. The fundamentally three-dimensional origami folding imposes a unique kinematic constraint onto the deformations of these two unit cells. This constraint can be estimated based on a mismatch between the spine angles of these two cells and an equivalent constraint stiffness coefficient. Our analysis shows that when the folding-induced kinematic constraint strengthens (aka. constraint stiffness increases), the potential energy barrier of compressing the dual cell assembly from a certain stable state to another is significantly increased, however, the energy barrier of the opposite extension does not change as much. As a result, one needs to apply a large force to compress the origami cellular structure but only a small force to stretch it, hence the mechanical diode behavior. The results of this study, combined with the authors' previous work on the mechanical diode in tension, can open new avenues towards multi-functional structures and material systems capable of motion rectifying, wave propagation control, and mechanical computation.

Acknowledgment

The authors acknowledge the partial support from the National Science Foundation (Award # CMMI-1633952, 1751449 CAREER) and Clemson University (via startup funding and the CECAS Dean's Faculty Fellow Award).

References

[1] Oh, Y. S., and Kota, S., 2009, "Synthesis of Multistable Equilibrium Compliant Mechanisms Using Combinations of Bistable Mechanisms," J. Mech. Des., **131**(2), p. 021002.

[2] Harne, R. L., Wu, Z., and Wang, K. W., 2015, "Designing and Harnessing the Metastable States of a Modular Metastructure for Programmable Mechanical Properties Adaptation," J. Mech. Des., **138**(2), p. 021402.

[3] Harne, R. L., and Wang, K. W., 2013, "A Review of the Recent Research on Vibration Energy Harvesting via Bistable Systems," Smart Mater. Struct., **22**(2), p. 023001.

[4] Daqaq, M. F., Masana, R., Erturk, A., and Dane Quinn, D., 2014, "On the Role of Nonlinearities in Vibratory Energy Harvesting: A Critical Review and Discussion," Appl. Mech. Rev., **66**(4), p. 040801.

[5] Frenzel, T., Findeisen, C., Kadic, M., Gumbsch, P., and Wegener, M., 2016, "Tailored Buckling Microlattices as Reusable Light-Weight Shock Absorbers," Adv. Mater., **28**(28), pp. 5865–5870.

[6] Puglisi, G., and Truskinovsky, L., 2002, "Rate Independent Hysteresis in a Bi-Stable Chain," J. Mech. Phys. Solids, **50**(2), pp. 165–187.

[7] Shan, S., Kang, S. H., Raney, J. R., Wang, P., Fang, L., Candido, F., Lewis, J. A., and Bertoldi, K., 2015, "Multistable Architected Materials for Trapping Elastic Strain Energy," Adv. Mater., **27**(29), pp. 4296–4301.

[8] Harne, R. L., and Wang, K. W., 2014, "A Bifurcation-Based Coupled Linear-Bistable System for Microscale Mass Sensing," J. Sound Vib., **333**(8), pp. 2241–2252.

[9] Harne, R. L., and Wang, K. W., 2015, "Passive Measurement of Progressive Mass Change via Bifurcation Sensing with a Multistable Micromechanical System," J. Intell. Mater. Syst. Struct., **26**(13), pp. 1622–1632.

[10] Emam, S. A., and Inman, D. J., 2015, "A Review on Bistable Composite Laminates for Morphing and Energy Harvesting," Appl. Mech. Rev., **67**(6), p. 060803.

[11] Li, S., Fang, H., Sadeghi, S., Bhovad, P., and Wang, K. W., 2018, "Architected Origami Materials: How Folding Creates Sophisticated Mechanical Properties," Adv. Mater., p. to appear.

[12] Schenk, M., and Guest, S. D., 2013, "Geometry of Miura-Folded Metamaterials," Proc. Natl. Acad. Sci., **110**(9), pp. 3276–3281.

[13] Wei, Z. Y., Guo, Z. V, Dudte, L. H., Liang, H. Y., and Mahadevan, L., 2013, "Geometric Mechanics of Periodic Pleated Origami," Phys. Rev. Lett., **110**(21), p. 215501.

[14] Fang, H., Li, S., Ji, H., and Wang, K. W., 2016, "Uncovering the Deformation Mechanisms of Origami Metamaterials by Introducing Generic Degree-Four Vertices," Phys. Rev. E, **94**(4), p. 043002.

[15] Fang, H., Li, S., and Wang, K. W., 2016, "Self-Locking Degree-4 Vertex Origami Structures," Proc. R. Soc. A Math. Phys. Eng. Sci., **472**(2195), p. 20160682.

[16] Fang, H., Chu, S. A., Xia, Y., and Wang, K. ., 2018, "Programmable Self-Locking Origami Mechanical Metamaterials," Adv. Mater., p. 1706311.

[17] Lv, C., Krishnaraju, D., Konjevod, G., Yu, H., and Jiang, H., 2014, "Origami Based Mechanical Metamaterials," Sci. Rep., **4**, p. 5979.

[18] Waitukaitis, S., Menaut, R., Chen, B. G., and van Hecke, M., 2015, "Origami Multistability: From Single Vertices to Metasheets," Phys. Rev. Lett., **114**(5), p. 055503.

[19] Li, S., and Wang, K. W., 2015, "Fluidic Origami with Embedded Pressure Dependent Multi-Stability : A Plant Inspired Innovation," J. R. Soc. Interface, **12**(111), p. 20150639.

[20] Cai, J., Deng, X., Ya, Z., Jiang, F., and Tu, Y., 2015, "Bistable Behavior of the Cylindrical Origami Structure with Kresling Pattern," J. Mech. Des., **137**(6), p. 061406.

[21] Nayakanti, N., Tawfick, S. H., and Hart, J. A., 2018, "Twist-Coupled Kirigami Cells and Mechanisms," Extrem. Mech. Lett., **21**, pp. 17–24.

[22] Silverberg, J. L., Na, J. H., Evans, A. A., Liu, B., Hull, T. C., Santangelo, C. D., Lang, R. J., Hayward, R. C., and Cohen, I., 2015, "Origami Structures with a Critical Transition to Bistability Arising from Hidden Degrees of Freedom," Nat. Mater., **14**(4), pp. 389–393.
[23] Sengupta, S., and Li, S., 2018, "Harnessing the Anisotropic Multistability of Stacked-Origami Mechanical Metamaterials for Effective Modulus Programming," J. Intell. Mater. Syst. Struct., **29**(14), pp. 2933–2945.
[24] Fang, H., Wang, K. W., and Li, S., 2017, "Asymmetric Energy Barrier and Mechanical Diode Effect from Folding Multi-Stable Stacked-Origami," Extrem. Mech. Lett., **17**, pp. 7–15.